ADVANCED FUNCTIONAL MATERIALS
www.afm-journal.de

Fast-Response, Stiffness-Tunable Soft Actuator by Hybrid Multimaterial 3D Printing

Yuan-Fang Zhang, Ningbin Zhang, Hardik Hingorani, Ningyuan Ding, Dong Wang, Chao Yuan, Biao Zhang, Guoying Gu, and Qi Ge**

Soft robots have the appealing advantages of being highly flexible and adaptive to complex environments. However, the low-stiffness nature of the constituent materials makes soft robotic systems incompetent in tasks requiring relatively high load capacity. Despite recent attempts to develop stiffness-tunable soft actuators by employing variable stiffness materials and structures, the reported stiffness-tunable actuators generally suffer from limitations including slow responses, small deformations, and difficulties in fabrication with microfeatures. This work presents a paradigm to design and manufacture fast-response, stiffness-tunable (FRST) soft actuators via hybrid multimaterial 3D printing. The integration of a shape memory polymer layer into the fully printed actuator body enhances its stiffness by up to 120 times without sacrificing flexibility and adaptivity. The printed Joule-heating circuit and fluidic cooling microchannel enable fast heating and cooling rates and allow the FRST actuator to complete a softening–stiffening cycle within 32 s. Numerical simulations are used to optimize the load capacity and thermal rates. The high load capacity and shape adaptivity of the FRST actuator are finally demonstrated by a robotic gripper with three FRST actuators that can grasp and lift objects with arbitrary shapes and various weights spanning from less than 10 g to up to 1.5 kg.

1. Introduction

Soft actuators and robots made of intrinsically soft and/or extensible materials have gained great attention due to their excellent capability of adapting to complex environments and building safe, coexisting interaction with humans.[1,2] They have found various applications in robotic manipulators,[3–6] crawling and swimming robots,[7–11] minimally invasive surgery devices,[12,13] and other biomedical systems.[14–18] However, the inherent low stiffness of constituent materials (for example, silicone elastomers) makes soft robotic systems incompetent in tasks requiring relatively high load capacity such as grasping and manipulation of heavy objects,[19] hand rehabilitation,[16] and precise surgical operations.[12,13]

In order to realize high load capacity during loading–carrying tasks while not sacrificing the compliance of soft actuators and robots during robot–object interaction, many efforts have been made to apply stiffness-tunable materials and structures to soft robotic systems.[20] These materials include shape memory polymers (SMPs),[21–27] electrorheological materials,[28,29] low melting point alloys (LMPAs),[30–33] granular or laminar jamming structures,[12,34–36] and elastomers filled with electro/magneto-active liquids.[37–39] Among them, thermally activated SMPs are one of the most promising stiffness-tunable materials due to the capability of reversibly changing the stiffness by three orders of magnitude from a few MPa to a few GPa during the transition from the soft rubbery state to the stiff glassy state.[40] Additionally, recent studies have demonstrated that (meth)acrylate-based SMPs possess good compatibility with 3D printing which significantly simplifies the manufacturing process, enriches the geometric complexity of SMP structures, and offers the possibility of directly 3D printing robots.[41–44]

Some recent works have been devoted to applying SMPs to soft actuators, especially pneumatic ones, to realize stiffness tunability.[22–24,26,27] For example, Takashima et al. reported a pneumatic artificial rubber muscle by embedding resistive wires into an SMP layer for tailoring the bending motion.[22] By using fused deposition modeling (FDM)-based 3D printing, Chen and co-workers pioneered the methods in fabricating soft

Dr. Y.-F. Zhang, H. Hingorani, Dr. D. Wang, Dr. C. Yuan, Dr. B. Zhang, Prof. Q. Ge
Digital Manufacturing and Design Centre
Singapore University of Technology and Design
Singapore 487372, Singapore
E-mail: ge_qi@sutd.edu.sg
N. Zhang, N. Ding, Prof. G. Gu
Soft Robotics and Biodesign Lab
Robotics Institute
School of Mechanical Engineering
Shanghai Jiao Tong University
Shanghai 200240, China
E-mail: guguoying@sjtu.edu.cn
Prof. G. Gu
State Key Laboratory of Mechanical System and Vibration
Shanghai Jiao Tong University
Shanghai 200240, China
Prof. Q. Ge
Science and Math Cluster
Singapore University of Technology and Design
Singapore 487372, Singapore
The ORCID identification number(s) for the author(s) of this article can be found under https://doi.org/10.1002/adfm.201806698.

DOI: 10.1002/adfm.201806698

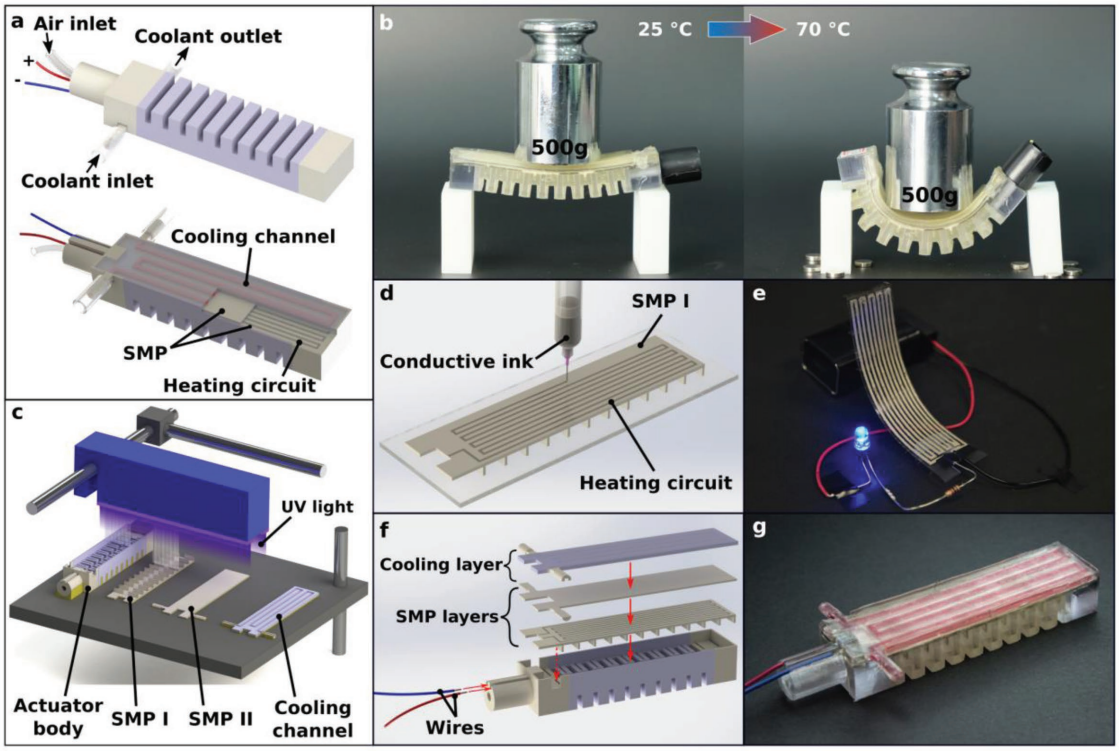

Figure 1. FRST soft actuator made by hybrid multimaterial 3D printing technologies. a) Schematics of the FRST soft actuator enabled by integrating a Joule-heating circuit and a fluidic cooling microchannel onto a stiffness-tunable SMP layer. b) Demonstration of the stiff–soft duality of the FRST soft actuator between 25 and 70 °C. c) Illustration of fabricating the four separate parts of an FRST soft actuator on a Polyjet multimaterial 3D printer. d) Printing the deformable Joule-heating circuit on SMP I via DIW. e) Demonstration of the flexibility of the printed Joule-heating circuit. f) Assembling the four separate parts to form FRST actuator. g) An assembled FRST soft actuator with a highlighted fluidic microchannel.

actuators with SMP components as stiffness-tunable layers or joints.[23,24,26] Buckner et al. introduced a conductive SMP epoxy composite to achieve stiffness tunability on a pneumatic actuator.[27] While the reported SMP-based soft actuators have explored the feasibility of stiffness tuning, they generally suffer from limitations such as slow responses (especially in the cooling process), small deformations, and difficulties in automated fabrications with microfeatures.[45]

In this article, we report a paradigm to design and manufacture a type of fast-response, stiffness-tunable (FRST) soft actuator using hybrid multimaterial 3D printing technologies. In **Figure 1**a, we present the schematic of the fully 3D-printed FRST soft actuator with a pneumatic body and an embedded SMP inextensible layer. The integration of the SMP not only maintains the flexibility and adaptability of the actuator (when the SMP layer is soft at 70 °C), but also significantly enhances the stiffness of the FRST actuator (when the SMP layer becomes stiff at 25 °C) by up to about 120 times compared with that of its purely elastomeric counterpart. In Figure 1b, we demonstrate the stiff–soft duality of the FRST actuator by placing a 500 g weight on its inextensible layer side. At room temperature, it is stiff enough to support the weight; while at 70 °C, it becomes soft, and the weight leads to a large bending of the actuator. Besides the stiffness tunability, more importantly, the FRST actuator demonstrates fast-response rates in heating and cooling. It can reversibly switch its stiffness between 10 MPa and ≈1 GPa within 32 s. We realize the fast heating with a rate of 4.5 °C s^{-1} (i.e., heating from 25 to 70 °C within 10 s) through printing a deformable, conductive Joule-heating circuit in the SMP layer. On top of the SMP layer, we print a deformable layer with a fluidic microchannel allowing a fast cooling rate of 2.0 °C s^{-1} (cooling from 70 to 25°C within 22 s). To our best knowledge, our FRST soft actuator exhibits the fastest heating and cooling rates among all the reported soft actuators that realize the stiffness tunability using thermally responsive stiffness-tunable materials such as SMPs, shape memory alloys (SMAs), LMPAs. In addition, we implemented a multibranch viscoelastic model of the SMP into the FRST actuator structure to simulate the entire working cycle, including the heat transfer as well as the stiffness changes of the SMP layer. The simulations guide the structure design of FRST actuator and provide insights into enhancement of load capacity with increased SMP thickness and the consequent cost in heating–cooling time. To demonstrate the applications of the developed FRST actuator, we integrate a stiffness-tunable gripper with three FRST actuators into an industrial robot. The experiments demonstrate that our gripper is capable of grasping and lifting various objects (such as ping-pong balls, vegetables, fruits, bulbs, and dumbbells) with different geometries and weights ranging from a few grams up to 1.5 kg. The designs of the Joule-heating circuit and the fluidic microchannel layer greatly reduce the period of a heating–cooling cycle to about 30 s, which significantly enhances the practicability of the thermally responsive stiffness-tunable soft actuator, rendering it suitable to further applications.

2. Results and Discussions

2.1. Manufacturing Processes

As shown in Figure 1c, we start the fabrication of an FRST soft actuator by using a commercial Polyjet multimaterial 3D printer (J750, Stratasys Ltd., Eden Prairie, MN, USA) to print the four separate parts: the body of the soft pneumatic actuator, two SMP slices (SMP I and II) with the same thickness, and an elastomeric layer with a fluidic microchannel for cooling. The actuator body with inflatable chambers follows the design of the fast-pneumatic network bending actuator[46] and is printed with an elastomeric material. The two ends of the actuator body are made of a rigid material to ensure the leak tightness of the assembled prototype. In this work, we use Agilus30 (Stratasys Ltd., Eden Prairie, MN, USA) as the elastomer and VeroClear (Stratasys Ltd., Eden Prairie, MN, USA) as the SMP slices and the rigid ends of the actuator body. The geometric details on the four parts are available in Figure S1 in the Supporting Information (Section S1, Supporting Information).

To provide fast-rate localized Joule-heating, we print a deformable conductive circuit with a silver nanoparticle (Ag NP) ink (ME603, DuPont Inc., Wilmington, DE, USA) on top of the SMP Slice I via direct ink writing (DIW) (Figure 1d and see Section S2 in the Supporting Information for details). The printing parametric studies will be discussed in Section 2.4. After the DIW process, the SMP slice I with the heating circuit is placed in a universal oven (UF55, Memmert GmbH + Co. KG, Germany) at 80 °C for 60 min to sinter the Ag NP circuit to obtain adequate deformability while maintaining its conductivity for the application of a pneumatic actuator (Figure 1e).[47] As illustrated in Figure 1f, the printed Joule-heating circuit is sandwiched by another SMP slice (SMP II) to ensure even heat diffusion. We stack all the four printed parts and bond them with VeroClear polymer solution, followed by UV curing (see details in Section S2 in the Supporting Information). Figure 1g presents the still image of an assembled FRST soft actuator where the layout of the cooling microchannel is highlighted with a red fluid.

2.2. Stiffness-Tunable Behavior of the SMP Material

To investigate the thermomechanical behavior of the SMP material (i.e., VeroClear), we performed a dynamic mechanical analysis (DMA) test on an DMA analyzer (Q800, TA Instrument Inc., New Castle, DE, USA) by decreasing the temperature from 90 to −30 °C at a rate of 2 °C min^{-1}. We identified the glass transition temperature T_g of the SMP material to be around 60 °C according to the peak of tanδ (the ratio between the loss modulus and storage modulus). **Figure 2**a shows that the storage modulus (corresponding to elastic response) increases remarkably from ≈10 MPa at high temperatures (>70 °C) to more than 1 GPa at room temperature due to the glass transition from the rubbery state to the glassy one.[48,49] We also used a multibranch thermoviscoelastic model (see Section S3 in the Supporting Information) to describe the temperature-dependent stiffness of the SMP based on the DMA

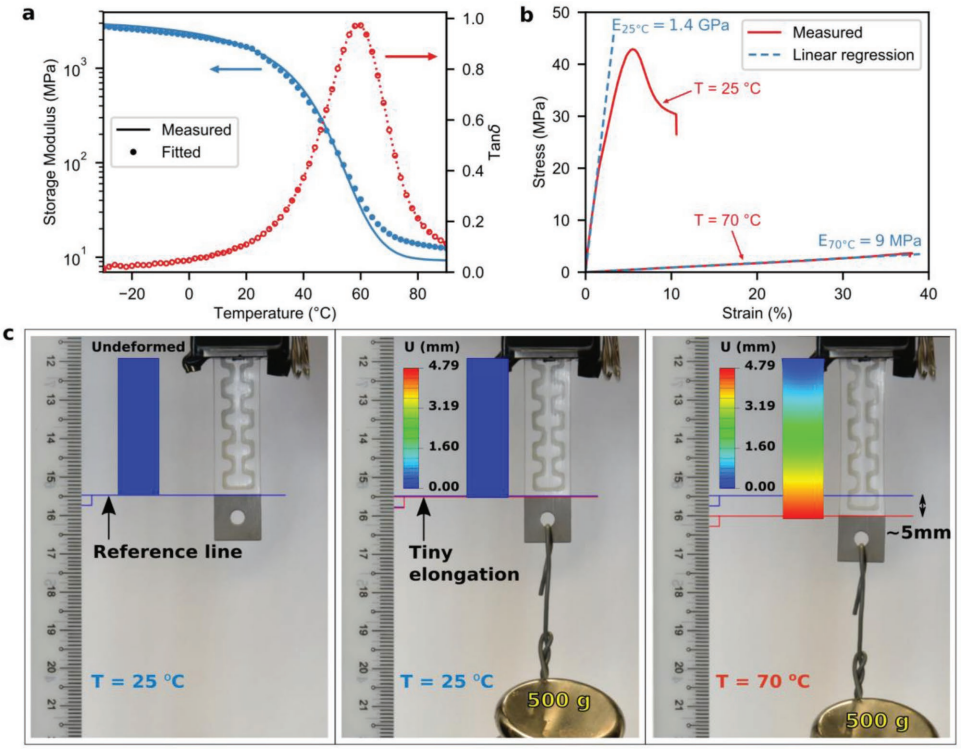

Figure 2. Stiffness-tunable behavior of the SMP material. a) The DMA characterization of VeroClear which is chosen as the SMP material. b) Stress–strain curves of VeroClear at 25 and 70 °C. c) Demonstration of the stiffness variation of the thermally activated SMP material. The variable *U* describes the local displacement in the vertical direction.

results (Figure 2a).[50–53] The model was later implemented into the geometry of the FRST actuator to guide its design. We further examined the temperature-dependent stiffness variation of the SMP by conducting uniaxial tensile tests on a mechanical testing machine (MTS) (Eden Prairie, MN, USA) with a strain rate of 0.005 s^{-1} (see Section S4 in the Supporting Information). The results indicate that the SMP exhibits a linear stress–strain behavior with a modulus of 9 MPa at 70 °C, and its stiffness dramatically increases to 1.4 GPa when the temperature drops to 25 °C (Figure 2b). The stiffness variation observed from the quasi-static uniaxial tensile tests agrees well with that from DMA tests.

In Figure 2c, we demonstrated the stiffness variation of the thermally activated SMP by hanging a 500 g weight onto an SMP strip where a conductive Ag NP circuit of 1.2 Ω was printed on one side of the strip (see Section S5 in the Supporting Information). At room temperature, the SMP strip has sufficient stiffness to balance the 500 g weight with nearly invisible deformation. The finite-element (FE) simulation on ABAQUS (V6.14, Dassault Systèmes Simulia Corp., Providence, RI, USA) indicates that the deformation is about 0.1% as determined by the ratio of the vertical displacement U on the lower end of the strip to its original length of 40 mm (see Section S7 in the Supporting Information). When the SMP strip is heated to 70 °C after applying a 1.4 A current to the circuit for about 10 s, it becomes soft and deforms by 12% of strain under the 500 g weight. The FE simulations yield results in good agreement with the experiments, thus validating the aforementioned multibranch thermoviscoelastic model. A video of this demonstration is available in Movie S1 in the Supporting Information.

2.3. Characterization on Load Capacity

Figure 3a illustrates a typical working cycle that enables the stiffness-tunable actuation of the FRST soft actuator. The working cycle includes five steps: i) softening the actuator by heating the SMP layer with the conductive circuit; ii) bending the actuator by applying pressurized air; iii) stiffening the actuator by cooling the SMP layer with cold water of 4 °C driven through the elastomeric microchannel with a peristaltic pump; iv) carrying a heavy load even after releasing the pressurized air; v) recovering to the straight configuration by heating the SMP layer. Figure 3b presents time-lapse images from the video of a stiffness-tunable actuation experiment (Movie S2, Supporting Information). The results demonstrate that our FRST soft actuator can rapidly and reversibly switch between the stiff and soft states by heating and cooling the SMP layer, respectively. At the soft state, our actuator can bend to more than 90° under an air pressure of 50 kPa; at the stiff state, our actuator can carry a high payload of 100 g on its tip. To further investigate this stiffness-tunable actuation, we conducted an FE simulation by implementing the multibranch thermoviscoelastic model into the SMP layer of the FRST actuator. In Figure 3c, the FE simulation agrees very well with the experiment. Notably, in the loading–carrying step, a slight deformation of the actuator is observed from both the experiment and the simulation. Moreover, the simulation demonstrates that the SMP layer carries most of the load and the stress on the soft part of the actuator is negligible. Details about the FE simulation can be found in Section S7 in the Supporting Information.

In order to quantitatively investigate the tunable stiffness, we built a bending stiffness characterization system to compare the initial bending stiffness of our FRST soft actuator (Figure 3d and see details in Section S6 in the Supporting Information). We used a temperature regulation system that controlled the power supply for the heating circuit to keep the temperature constant throughout a test. During a bending stiffness test, the horizontal linear stage moved by 5 mm at 0.5 mm s^{-1}, which drove the load cell to push the distal end of the actuator. A constraining platform was placed near the bellow side of the actuator to prevent buckling due to the structural instability caused by the tip loading on a pressurized soft pneumatic actuator.[54]

We performed bending stiffness characterizations for three actuators: i) a purely soft pneumatic actuator (Figure 3e); ii) an FRST actuator with a heated, soft SMP layer (Figure 3f); iii) an FRST actuator with a cold, stiff SMP layer (Figure 3g). As shown in Figure 3e, although there are only slight changes on the initial bending stiffness k (≈4 mN mm^{-1}, the slope of the curve at displacement less than 1 mm) under different applied pressures, the initial force (the force at zero displacement) exerted on the actuator increases remarkably with the increase in applied pneumatic pressure (i.e., 0, 25, and 50 kPa). In the case under the 50 kPa applied pressure, the force–displacement curve exhibits a pronounced nonlinear characteristic. At 5 mm displacement, the force exerted on the actuator increases significantly from 14 to 73 mN by augmenting the applied pneumatic pressure from 0 to 50 kPa. Figure 3f presents the force–displacement curves for the FRST actuator with a heated soft SMP layer. The trends of the force–displacement curves under different applied pressures are the same as those of the purely soft pneumatic actuator. However, the initial bending stiffness increases to ≈20 mN mm^{-1} as the heated soft SMP layer is 13 times stiffer than the elastomeric inextensible layer made of Agilus30 (see details in Figure S3 in the Supporting Information [Section S4, Supporting Information]). We further calculate the net force used to push the distal end of the actuator by 5 mm displacement by deducting the initial force (at zero displacement) from the maximum force (at 5 mm displacement) in Figures 3e,f. It is found that the higher stiffness of the inextensible layer made of the heated soft SMP also leads to an increase in the net force from 73 mN at 50 kPa (14 mN at 0 kPa) to 333 mN at 50 kPa (80 mN at 0 kPa). With a cold stiff SMP layer, the initial bending stiffness is enhanced to 292 mN mm^{-1} as the modulus of the inextensible layer increases to 1.4 GPa (Figure 3g). Different from the results with soft elastomer and heated soft SMP layers (Figure 3e,f), the initial force of the FRST actuator with a stiff SMP layer starts at 0 mN and is independent on the applied pressure. This is because even a 50 kPa air pressure is not sufficient to bend the actuator with a stiff inextensible layer of 1.4 GPa. Under different applied pressures, the force on the actuator at 5 mm displacement reaches about 1350 mN.

Figure 3h,i compares the initial bending stiffnesses and the forces at 5 mm displacement for all three actuators. When the purely soft inextensible layer is replaced by the stiff SMP layer, the initial bending stiffness is enhanced by about 120 times at 0 kPa pneumatic pressure from 2.4 to 288 mN mm^{-1}. When a

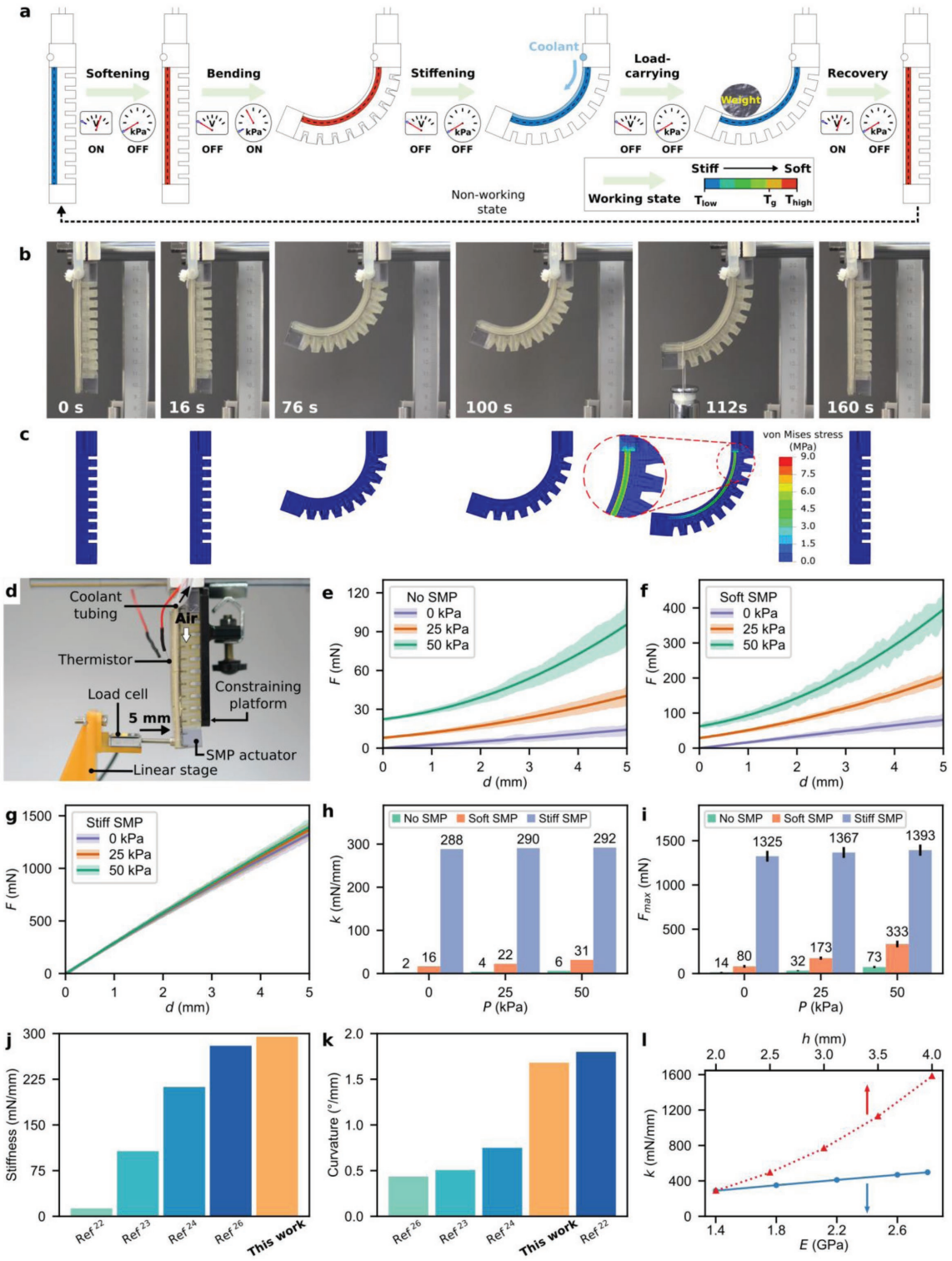

Figure 3. Characterization on load capacity of an FRST soft actuator. a) Typical working cycle of the actuator. The "odometer-type" schematics represent the ON/OFF states of the Joule-heating circuit and the applied pneumatic pressure, respectively. b) Time-lapse images during the working cycle. c) FE simulation results in a typical working cycle. d) Experimental setup for the load capacity characterization. e–g) Tip output force F plotted as function of tip displacement d on actuator with respect to no SMP, soft SMP, and stiff SMP components inflated with pneumatic pressures of 0, 25, and 50 MPa, respectively. The measured data are plotted as bands and the curves fitted with a second-order polynomial method are plotted as solid lines. h) Comparison of initial bending stiffnesses k in all the tested scenarios. i) Comparison of maximum output forces F_{max} in all the tested scenarios. j,k) Comparison of stiffness and curvature with relevant works in the literature. l) Predicted influences of SMP thickness h and modulus E on the initial bending stiffness k via FE simulations.

50 kPa pneumatic pressure is applied, the initial bending stiffness is enhanced by 50 times from 6.3 to 292 mN mm^{-1}. Similarly, after replacing the purely soft inextensible layer with the stiff SMP layer, the force at 5 mm displacement increases by about 100 times at 0 kPa pneumatic pressure from 14 to 1325 mN and 19 times at 50 kPa pneumatic pressure from 73 to 1393 mN. Compared with previously reported SMP-enabled stiffness-tunable soft actuators,[22–24,26] our FRST soft actuator has advantages in both initial bending stiffness (Figure 3j) and bendability (Figure 3k).

For further improvements, we used computational tools to investigate the influences of SMP layer thickness and material modulus on the resulting bending stiffness. Predicted results from FE simulations as shown in Figure 3l (see details in Section S7 in the Supporting Information) indicate that an increase of more than four times in bending stiffness can be achieved by doubling the SMP layer thickness h, whereas doubling the elastic modulus E of the material is less efficient in improving the actuator's load capacity.

2.4. Characterization on Heating and Cooling Efficiencies

In order to realize fast heating to the SMP layer, we start the design of the heating circuit by calculating the Joule-heating power which determines the heating rate. The power follows the formula $P = I^2R$, where I is the current and R is the resistance of the heating circuit.[55] Upon a constant current, the power is proportional to R which can be calculated as $R = \rho \cdot l \cdot A^{-1}$, where ρ is the resistivity, l is the length, and A is the cross-sectional area.[55] ρ is the intrinsic property of the Ag NP forming the circuit and is dependent on the sintering conditions.[47] Thus, the resistance as well as the heating power can be increased by increasing l and/or reducing A which are the geometric parameters of a printed circuit. As introduced in Figure 1d, the Ag NP wire was printed using the DIW printing system where the printing speed and dispensing pressure are the two key parameters to control the geometric parameters of a printed circuit. For this reason, we performed printing characterizations to investigate the effects of the printing speed and dispensing pressure on the widths and electrical resistances of sample wires printed on VeroClear substrates. Details about the printing characterizations are available in Section S9 in the Supporting Information. **Figure 4**a plots the variations of the width of printed lines upon changes of printing speed and dispensing pressure. Overall, the width decreases with an increase in printing speed and a decrease in dispensing pressure. However, the width cannot be infinitely small. When the width approaches ≈0.8 mm, further increasing the

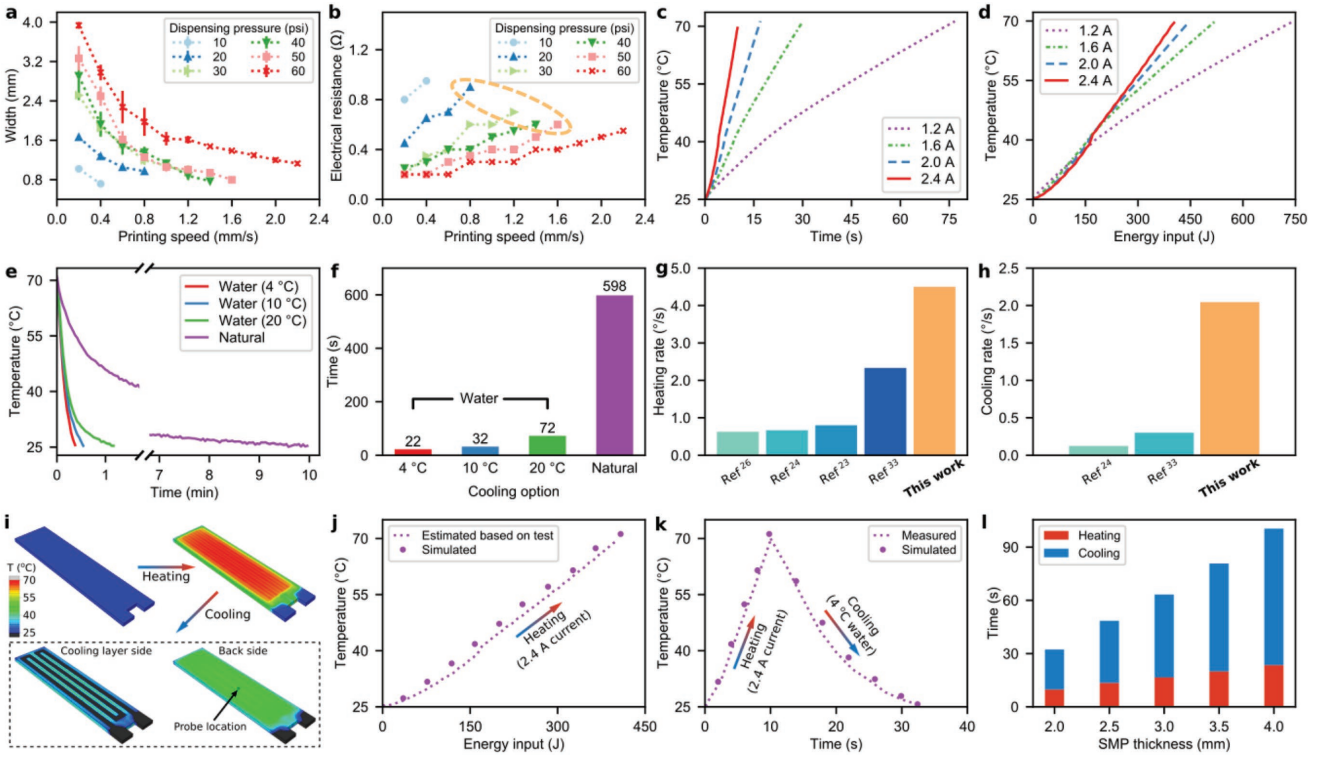

Figure 4. Characterization on heating and cooling efficiencies. a,b) Width and electrical resistance, respectively, of sample circuit line as functions of printing speed and dispensing pressure. c,d) Temperature–time and temperature–energy relationships, respectively, from heating tests of SMP from 25 to 70 °C with different current values. e) Temperature–time relationship from cooling tests of SMP from 70 to 25 °C with water at different temperatures and natural cooling. f) Comparison of durations required to reduce the temperature of SMP from 70 to 25 °C with different cooling options. g,h) Comparisons of, respectively, heating and cooling rates with the values reported in relevant references. i) Schematic of thermal–electrical FE model simulating the heating and cooling processes. The temperature field is shown with appropriate colormap. j) Comparison of simulated and measured temperature–energy relationships at the probe location during heating with 2.4 A current. k) Comparison of simulated and measured temperature–time relationships during a heating–cooling cycle. l) Simulated heating and cooling times for different thicknesses of SMP layer.

printing speed or decreasing the dispensing pressure leads to discontinuous printed wires (Figure S6, Supporting Information). In Figure 4b, we also measured the electrical resistance values of the printed sample wires. Opposite to the effects of printing speed and dispensing pressure on the width, the electrical resistance increases with increasing printing speed and decreasing dispensing pressure. The circled combinations of parameters in Figure 4b are found suitable to our application as they result in relatively small wire width of ≈0.8 mm and reasonably large resistance values between 0.6 and 0.9 Ω for sample wires measuring 4 cm in length. In the circuit printing, we opted for the combination of 1.6 mm s^{-1} printing speed and 50 psi dispensing pressure to save printing time. The printed circuit pattern is presented in Figure 1e and Figure S4 in the Supporting Information, where the spacing between two lines is 0.8 mm to maximize the wire length and the area that the circuit can cover while ensuring enough spacing to avoid unwanted connection between two neighboring lines.

We investigated the effect of the applied current on the heating rate by measuring the temperature variations of the SMP layer. For this purpose, we attached an ultraminiature thermistor (B57540G1, EPCOS AG, Germany) to the center of the innermost surface of the SMP component (Figure S4, Supporting Information). Details about the interpolation of the resistance–temperature relationship are given in Section S8 in the Supporting Information. As shown in Figure 4c, the time to heat the SMP layer from 25 to 70 °C is reduced from 75 to 10 s by increasing the current from 1.2 to 2.4 A. In general, the current can be further increased to reduce the heating time, but the effect is limited as the heat diffusion from the circuit to the SMP layer also takes time, and the further increase in current may cause the burnout of the circuit due to excessive heating. To better understand the heating process, we calculated the heating energy Q generated from the printed circuit through Joule's law $Q = I^2Rt$. Figure 4d presents the temperature–energy relationship under different applied currents. The resulting curves plotted in Figure 4d coincide in the temperature range from 25 to 40 °C and then gradually diverge. The fact that a lower current requires more energy input to heat the SMP to a higher temperature could be caused by the energy dissipation over a longer heating process.

The FRST actuator utilizes the fluidic microchannel cooling system to significantly improve the cooling rate whereas existing stiffness-tunable soft actuators relied on slow convection cooling.[26,33] To characterize the cooling rates of the FRST actuator, we conducted tests by using water coolant at different temperatures, 4, 10, and 20 °C, respectively. The flow rate of water was kept at 70 mL min^{-1} using a peristaltic pump (KCP-C, Kamoer Fluid Tech Co. Ltd., China). For comparison, we also tested cooling process by natural convection. Figure 4e presents the temperature change over time under the different cooling options and Figure 4f summarizes the durations needed to reduce the temperature on an SMP layer from 70 to 25 °C. Compared with natural convection cooling which requires about 10 min, using water coolant at 4 °C takes only 22 s to decrease the temperature by 45 °C, which improves the cooling rate by 27 times. In Figure 4g,h, we compare the heating and cooling rates of the FRST actuator with values reported in relevant works in the literature.[23,24,26,33] To our best knowledge, the FRST actuator is the stiffness-tunable actuator with the fastest heating and cooling rates, and it is able to complete the heating–cooling cycle within 32 s.

As the FE simulations in Figure 3l suggest that the bending stiffness of the FRST actuator can be greatly increased by increasing the thickness of the SMP layer, it is necessary to understand how the heating and cooling durations are affected by the increase in the layer thickness. As shown in Figure 4i, we conducted coupled thermal–electrical analyses on ABAQUS to model the heating–cooling process (see details on modeling in Section S10 in the Supporting Information). The heating–cooling cycle realized with 2.4 A current and 4 °C water coolant, respectively, was used to validate the FE simulations. Figure 4j compares the heating simulation with experiment on the temperature–energy relationship, and Figure 4k compares the simulated and measured temperature–time relationships during a heating–cooling cycle. In general, the model simulates well the experiment. Using this validated model, we further predict the heating–cooling cycle

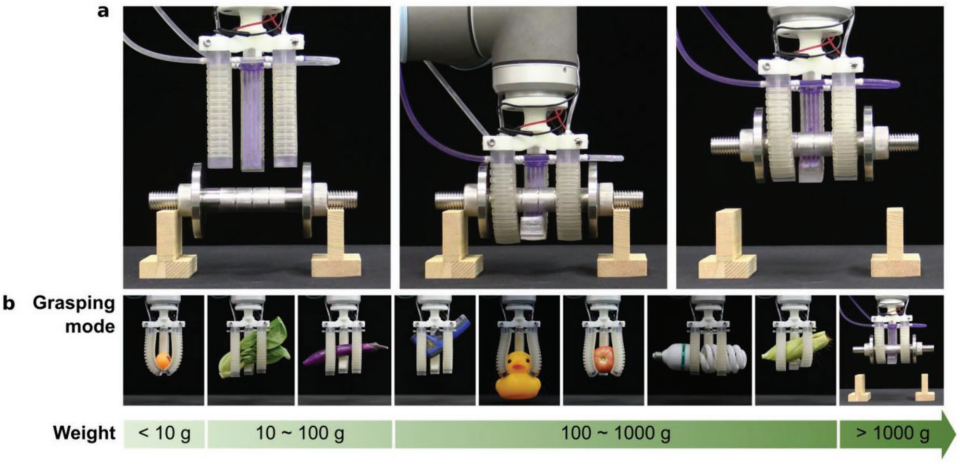

Figure 5. Demonstration of high load capacity and good shape adaptivity by a versatile gripper equipped with three FRST actuators. a) Grasping and lifting of a dumbbell weighing 1.5 kg. b) Grasping of objects with arbitrary shapes and various weights ranging from less than 10 g to 1.5 kg.

for FRST actuators with different thicknesses of the SMP layer. Figure 4l suggests that an increase in the SMP layer thickness from 2.0 to 4.0 mm results in an increase in heating duration from 10 to 24 s and the cooling duration from 22 to 77 s. Therefore, a threefold increase in the heating–cooling duration needs to be traded off for a fourfold enhancement in the bending stiffness.

2.5. Stiffness-Tunable Robotic Gripper Equipped with FRST Actuators

To further demonstrate the versatility of the FRST soft actuator, we develop a stiffness-tunable robotic gripper by assembling three FRST actuators to a 3D-printed base which is attached to an industrial robotic arm (UR10, Universal Robots, Denmark) for vertical motion. Both the heating circuits and the air inlet tubes are connected in parallel; the cooling microchannels are connected in series. The enhanced load capacity of the robotic gripper is demonstrated in **Figure 5**a where the robotic gripper is able to lift a 1.5 kg dumbbell (Movie S3, Supporting Information). The stiffness tunability of the FRST actuators makes the robotic gripper not only capable of carrying heavy loads but also able to conform to and lift objects with arbitrary shapes and various weights spanning from less than 10 g to above 1000 g as displayed in Figure 5b.

3. Conclusion

In summary, this article presents a paradigm to design and manufacture FRST soft actuators, benefiting from the thermomechanical properties of SMP and hybrid multimaterial 3D printing. We embed a SMP layer into a fully printed pneumatic soft actuator to enhance its stiffness by 120 times without sacrificing flexibility and adaptivity. Fast heating and cooling are realized by a printed deformable conductive circuit and a printed fluidic microchannel which enable the FRST actuator to complete a softening–stiffening (heating–cooling) cycle within 32 s. The high load capacity and good shape adaptivity are demonstrated by a robotic gripper equipped with three assembled FRST actuators that can grasp and lift objects of arbitrary shapes and various weights spanning from less than 10 g to up to 1.5 kg.

Supporting Information

Supporting Information is available from the Wiley Online Library or from the author.

Acknowledgements

Y.F.Z. and N.Z. contributed equally to this work. Y.F.Z., H.H., D.W., C.Y., B.Z., and Q.G. acknowledge support from SUTD Digital Manufacturing and Design Centre (DManD), and the National Additive Manufacturing Innovation Cluster (NAMIC). G.G. acknowledges support from the National Natural Science Foundation of China (Grants 51622506 and 91848204) and the Science and Technology Commission of Shanghai Municipality (Grant 16JC1401000). Q.G. and G.G. acknowledge the Research Project of State Key Laboratory of Mechanical System and Vibration MSV201802, Shanghai Jiaotong University, China. Q.G. acknowledges SUTD Start-up Research Grant.

Conflict of Interest

The authors declare no conflict of interest.

Keywords

3D printing, fast-response, soft robots, stiffness-tunable

Received: September 21, 2018
Revised: November 15, 2018
Published online:

[1] D. Rus, M. T. Tolley, *Nature* **2015**, *521*, 467.
[2] M. Wehner, R. L. Truby, D. J. Fitzgerald, B. Mosadegh, G. M. Whitesides, J. A. Lewis, R. J. Wood, *Nature* **2016**, *536*, 451.
[3] R. F. Shepherd, A. A. Stokes, R. M. D. Nunes, G. M. Whitesides, *Adv. Mater.* **2013**, *25*, 6709.
[4] R. V. Martinez, J. L. Branch, C. R. Fish, L. Jin, R. F. Shepherd, R. M. Nunes, Z. Suo, G. M. Whitesides, *Adv. Mater.* **2013**, *25*, 205.
[5] R. K. Katzschmann, A. D. Marchese, D. Rus, *Soft Rob.* **2015**, *2*, 155.
[6] R. Deimel, O. Brock, *Int. J. Robotics Research* **2016**, *35*, 161.
[7] A. Villanueva, C. Smith, S. Priya, *Bioinspiration Biomimetics* **2011**, *6*, 036004.
[8] R. F. Shepherd, F. Ilievski, W. Choi, S. A. Morin, A. A. Stokes, A. D. Mazzeo, X. Chen, M. Wang, G. M. Whitesides, *Proc. Natl. Acad. Sci. U. S. A.* **2011**, *108*, 20400.
[9] M. T. Tolley, R. F. Shepherd, B. Mosadegh, K. C. Galloway, M. Wehner, M. Karpelson, R. J. Wood, G. M. Whitesides, *Soft Rob.* **2014**, *1*, 213.
[10] A. D. Marchese, C. D. Onal, D. Rus, *Soft Rob.* **2014**, *1*, 75.
[11] W. Wang, J. Y. Lee, H. Rodrigue, S. H. Song, W. S. Chu, S. H. Ahn, *Bioinspiration Biomimetics* **2014**, *9*, 046006.
[12] Y. J. Kim, S. B. Cheng, S. Kim, K. Iagnemma, *IEEE Trans. Rob.* **2013**, *29*, 1031.
[13] M. Cianchetti, T. Ranzani, G. Gerboni, T. Nanayakkara, K. Althoefer, P. Dasgupta, A. Menciassi, *Soft Rob.* **2014**, *1*, 122.
[14] E. T. Roche, R. Wohlfarth, J. T. B. Overvelde, N. V. Vasilyev, F. A. Pigula, D. J. Mooney, K. Bertoldi, C. J. Walsh, *Adv. Mater.* **2014**, *26*, 1200.
[15] P. Polygerinos, Z. Wang, K. C. Galloway, R. J. Wood, C. J. Walsh, *Rob. Auton. Syst.* **2015**, *73*, 135.
[16] H. K. Yap, J. H. Lim, F. Nasrallah, J. C. Goh, R. C. Yeow, presented at *2015 IEEE Int. Conf. on Robotics and Automation (ICRA)*, Seattle, WA, USA, May **2015**.
[17] E. T. Roche, M. A. Horvath, I. Wamala, A. Alazmani, S. E. Song, W. Whyte, Z. Machaidze, C. J. Payne, J. C. Weaver, G. Fishbein, J. Kuebler, N. V. Vasilyev, D. J. Mooney, F. A. Pigula, C. J. Walsh, *Sci. Transl. Med.* **2017**, *9*, eaaf3925.
[18] M. Cianchetti, C. Laschi, A. Menciassi, P. Dario, *Nat. Rev. Mater.* **2018**, *3*, 143.
[19] H. K. Yap, H. Y. Ng, C. H. Yeow, *Soft Rob.* **2016**, *3*, 144.
[20] M. Manti, V. Cacucciolo, M. Cianchetti, *IEEE Rob. Autom. Mag.* **2016**, *23*, 93.
[21] G. Mcknight, R. Doty, A. Keefe, G. Herrera, C. Henry, *J. Intell. Mater. Syst. Struct.* **2010**, *21*, 1783.
[22] K. Takashima, K. Sugitani, N. Morimoto, S. Sakaguchi, T. Noritsugu, T. Mukai, *Smart Mater. Struct.* **2014**, *23*, 125005.

[23] Y. Yang, Y. H. Chen, Y. Wei, Y. T. Li, *J. Mech. Rob.* **2016**, *8*, 061010.
[24] Y. Yang, Y. Chen, Y. Li, M. Z. Q. Chen, Y. Wei, *Soft Rob.* **2017**, *4*, 147.
[25] A. Firouzeh, M. Salerno, J. Paik, *IEEE Trans. Rob.* **2017**, *33*, 765.
[26] Y. Yang, Y. Chen, Y. Li, Z. Wang, Y. Li, *Soft Rob.* **2017**, *4*, 338.
[27] T. L. Buckner, E. L. White, M. C. Yuen, R. A. Bilodeau, R. K. Kramer, presented at *2017 IEEE/RSJ Int. Conf. on Intelligent Robots and Systems (IROS)*, Vancouver, BC, Canada, September **2017**.
[28] C. Mavroidis, *Res. Nondestr. Eval.* **2002**, *14*, 1.
[29] A. Tonazzini, A. Sadeghi, B. Mazzolai, *Soft Rob.* **2016**, *3*, 34.
[30] W. L. Shan, T. Lu, C. Majidi, *Smart Mater. Struct.* **2013**, *22*, 085005.
[31] J. Shintake, B. Schubert, S. Rosset, H. Shea, D. Floreano, presented at *2015 IEEE/RSJ Int. Conf. on Intelligent Robots and Systems (IROS)*, Hamburg, Germany, September **2015**.
[32] I. M. Van Meerbeek, B. C. Mac Murray, J. W. Kim, S. S. Robinson, P. X. Zou, M. N. Silberstein, R. F. Shepherd, *Adv. Mater.* **2016**, *28*, 2801.
[33] Y. Hao, T. Wang, Z. Xie, W. Sun, Z. Liu, X. Fang, M. Yang, L. Wen, *J. Micromech. Microeng.* **2018**, *28*, 024004.
[34] E. Brown, N. Rodenberg, J. Amend, A. Mozeika, E. Steltz, M. R. Zakin, H. Lipson, H. M. Jaeger, *Proc. Natl. Acad. Sci. U. S. A.* **2010**, *107*, 18809.
[35] G. N. Cheng, B. M. Lobovsky, J. S. Keating, M. A. Setapen, I. K. Gero, E. A. Hosoi, D. K. Iagnemma, presented at *2012 IEEE Int. Conf. on Robotics and Automation (ICRA)*, Saint Paul, MN, USA, May **2012**.
[36] S. Y. Narang, J. J. Vlassak, D. R. Howe, *Adv. Funct. Mater.* **2018**, *28*, 1707136.
[37] C. Majidi, R. J. Wood, *Appl. Phys. Lett.* **2010**, *97*, 164104.
[38] N. Kellaris, V. Gopaluni Venkata, M. G. Smith, K. S. Mitchell, C. Keplinger, *Sci. Rob.* **2018**, *3*, eaar3276.
[39] E. Acome, S. K. Mitchell, T. G. Morrissey, M. B. Emmett, C. Benjamin, M. King, M. Radakovitz, C. Keplinger, *Science* **2018**, *359*, 61.
[40] T. Xie, *Polymer* **2011**, *52*, 4985.
[41] Q. Ge, H. J. Qi, M. L. Dunn, *Appl. Phys. Lett.* **2013**, *103*, 131901.
[42] Q. Ge, C. K. Dunn, H. J. Qi, M. L. Dunn, *Smart Mater. Struct.* **2014**, *23*, 094007.
[43] J. Wu, C. Yuan, Z. Ding, M. Isakov, Y. Mao, T. Wang, M. L. Dunn, H. J. Qi, *Sci. Rep.* **2016**, *6*, 24224.
[44] Q. Ge, A. H. Sakhaei, H. Lee, C. K. Dunn, N. X. Fang, M. L. Dunn, *Sci. Rep.* **2016**, *6*, 31110.
[45] L. Wang, Y. Yang, Y. Chen, C. Majidi, F. Iida, E. Askounis, Q. Pei, *Mater. Today* **2018**, *21*, 563.
[46] B. Mosadegh, P. Polygerinos, C. Keplinger, S. Wennstedt, R. F. Shepherd, U. Gupta, J. Shim, K. Bertoldi, C. J. Walsh, G. M. Whitesides, *Adv. Funct. Mater.* **2014**, *24*, 2163.
[47] Q. Mu, K. C. Dunn, L. Wang, L. M. Dunn, J. H. Qi, T. Wang, *Smart Mater. Struct.* **2017**, *26*, 045008.
[48] Q. Zhao, H. J. Qi, T. Xie, *Prog. Polym. Sci.* **2015**, *49*, 79.
[49] Z. Ding, C. Yuan, X. Peng, T. Wang, H. J. Qi, M. L. Dunn, *Sci. Adv.* **2017**, *3*, e1602890.
[50] K. K. Westbrook, P. H. Kao, F. Castro, Y. F. Ding, H. J. Qi, *Mech. Mater.* **2011**, *43*, 853.
[51] Q. Ge, X. F. Luo, C. B. Iversen, H. B. Nejad, P. T. Mather, M. L. Dunn, H. J. Qi, *Int. J. Solids Struct.* **2014**, *51*, 2777.
[52] K. Yu, Q. Ge, H. J. Qi, *Nat. Commun.* **2014**, *5*, 3066.
[53] C. Yuan, X. M. Mu, C. K. Dunn, J. Haidar, T. J. Wang, H. J. Qi, *Adv. Funct. Mater.* **2018**, *28*, 1705727.
[54] Y. Sun, X. Q. Liang, H. K. Yap, J. W. Cao, M. H. Ang, R. C. H. Yeow, *IEEE Rob. Autom. Lett.* **2017**, *2*, 985.
[55] C. Alexander, M. Sadiku, *Fundamentals of Electric Circuits*, 5th ed., McGraw-Hill Higher Education, New York City, NY, USA **2012**.